Article

Cascade of phase transitions and Dirac revivals in magic-angle graphene

https://doi.org/10.1038/s41586-020-2373-y

Received: 25 November 2019

Accepted: 23 April 2020

Published online: 11 June 2020

Check for updates

U. Zondiner[1,5], A. Rozen[1,5], D. Rodan-Legrain[2,5], Y. Cao[2], R. Queiroz[1], T. Taniguchi[3], K. Watanabe[3], Y. Oreg[1], F. von Oppen[4], Ady Stern[1], E. Berg[1], P. Jarillo-Herrero[2]✉ & S. Ilani[1]✉

Twisted bilayer graphene near the magic angle[1–4] exhibits rich electron-correlation physics, displaying insulating[3–6], magnetic[7,8] and superconducting phases[4–6]. The electronic bands of this system were predicted[1,2] to narrow markedly[9,10] near the magic angle, leading to a variety of possible symmetry-breaking ground states[11–17]. Here, using measurements of the local electronic compressibility, we show that these correlated phases originate from a high-energy state with an unusual sequence of band population. As carriers are added to the system, the four electronic 'flavours', which correspond to the spin and valley degrees of freedom, are not filled equally. Rather, they are populated through a sequence of sharp phase transitions, which appear as strong asymmetric jumps of the electronic compressibility near integer fillings of the moiré lattice. At each transition, a single spin/valley flavour takes all the carriers from its partially filled peers, 'resetting' them to the vicinity of the charge neutrality point. As a result, the Dirac-like character observed near charge neutrality reappears after each integer filling. Measurement of the in-plane magnetic field dependence of the chemical potential near filling factor one reveals a large spontaneous magnetization, further substantiating this picture of a cascade of symmetry breaking. The sequence of phase transitions and Dirac revivals is observed at temperatures well above the onset of the superconducting and correlated insulating states. This indicates that the state that we report here, with its strongly broken electronic flavour symmetry and revived Dirac-like electronic character, is important in the physics of magic-angle graphene, forming the parent state out of which the more fragile superconducting and correlated insulating ground states emerge.

When a system of interacting electrons is cooled to low temperatures, it gradually loses its high-energy degrees of freedom while developing correlations that give rise to new collective degrees of freedom. The result is a hierarchy of energy scales, where the effective degrees of freedom at each scale are built out of a subset of those of the preceding scale. Understanding the effective degrees of freedom and their correlations at higher energies is therefore foundational for understanding more fragile states that emerge at lower energies.

The recent discovery that twisted bilayer graphene (TBG) exhibits correlated insulating[3], superconducting[4,5] and ferromagnetic[7,8] phases has opened a playground for studying such strongly correlated states. For twist angles that approach a 'magic angle' (MA) of about 1.1°, the bands were predicted[1,2] to narrow down markedly[1,9,10], leading to a variety of possible symmetry-breaking ground states[11–17]. These bands, identified directly by spectroscopic[18–20] and capacitive measurements[21], were shown to broaden substantially owing to interactions[22–24], and to exhibit correlation-induced gaps at the Fermi energy[22,23,25] as well as lattice symmetry breaking[22,23,25]. Yet a key question remains: what is the nature of the correlated state at energy scales comparable to the band width that gives rise to the low-energy many-body ground states?

In this work, using scanning measurements of the local electronic compressibility, we show that the energy bands of magic-angle twisted bilayer graphene (MATBG) undergo a dramatic transformation near integer fillings. Starting at the charge neutrality point (CNP), the four spin/valley flavours exhibit a Dirac-like character. However, as integer fillings are approached, sharp transitions occur in which a single flavour takes all the carriers from its partially filled peers, 'resetting' them to the vicinity of the CNP. This results in a Sisyphean band filling—the electrons attempt to fill all flavours symmetrically, yet repeatedly slip back to the Dirac point, reviving their Dirac-like character. Near these transitions, the compressibility reveals an asymmetry of the electronic state: the compressibility is high below any of the transitions, and drops precipitously above them. This behaviour is observed at temperatures well above the onset of the correlated insulator and superconducting states, demonstrating that the state we reveal here—with its strongly broken electronic flavour symmetry and revived Dirac-like electronic

[1]Department of Condensed Matter Physics, Weizmann Institute of Science, Rehovot, Israel. [2]Department of Physics, Massachusetts Institute of Technology, Cambridge, MA, USA. [3]National Institute for Materials Science, Tsukuba, Japan. [4]Dahlem Center for Complex Quantum Systems and Fachbereich Physik, Freie Universität Berlin, Berlin, Germany. [5]These authors contributed equally: U. Zondiner, A. Rozen, D. Rodan-Legrain. ✉e-mail: pjarillo@mit.edu; shahal.ilani@weizmann.ac.il

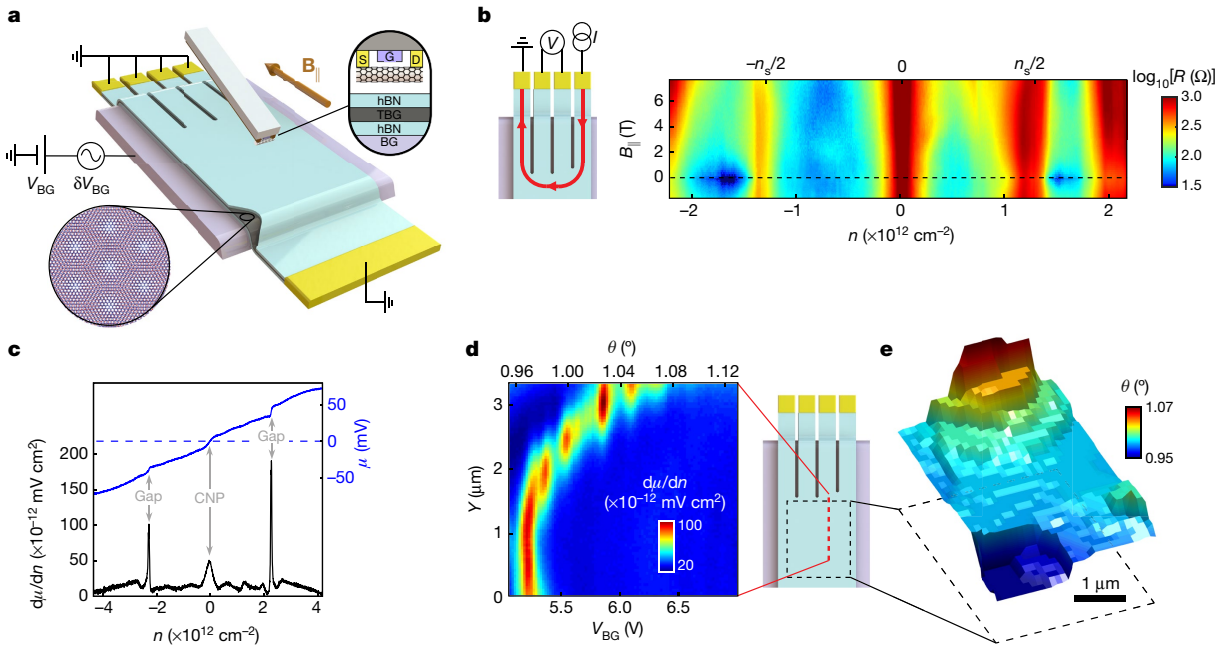

Fig. 1 | Measurement setup and device characterization. a, Twisted bilayer graphene (TBG) encapsulated between top and bottom hBN (blue), placed on a metallic back-gate (purple) and contacted by side contacts (yellow). We image the inverse electronic compressibility, $d\mu/dn$, using a scanning nanotube-based single electron transistor (SET; inset). (Here μ is the chemical potential of the carriers in the TBG and n is their density.) The SET measures the local $\delta\mu$ in response to a density modulation, δn, produced by an a.c. voltage on the back-gate, δV_{BG} (see Supplementary Information section 2). In these measurements the TBG is kept grounded, and a d.c. back-gate voltage, V_{BG}, sets the overall n. Some measurements use a parallel magnetic field, $B_\parallel$, whose orientation is indicated by the orange arrow. **b**, Four-probe resistance, R, measured using the top four contacts (left inset) as a function of carrier density, n, and $B_\parallel$, at $T = 50$ mK. The $\pm n_s/2$ labels on the top axis mark half-filled valence and conduction flat bands. **c**, Characteristic $d\mu/dn$ (black trace) and μ (blue trace, obtained by integrating the former) measured as function of n, at $T = 4$ K. Arrows mark the charge neutrality point (CNP) and the gaps separating the flat bands from the higher-energy dispersive bands. **d**, Measurement of $d\mu/dn$ as a function of a spatial coordinate, Y, along a line-cut across the sample (red dashed line, inset) and V_{BG} focusing on the peak at of $d\mu/dn$ that corresponds to a full flat band ($n = n_s$). The local twist angle, θ, is obtained directly from the back-gate voltage at which this peak appears (see text), and is indicated in the top y axis. In the centre of the sample, θ is rather homogeneous and smaller than the magic angle. In the top part of the sample, θ climbs in steps (fixed-θ domains) towards the MA. **e**, Spatial map of the twist angle, θ (covering the black dashed region in the inset), determined in a similar fashion to **d** but from a three-dimensional measurement of $d\mu/dn$ as a function of V_{BG}, X and Y (Supplementary Information section 4). A terraced landscape with constant-θ domains is visible. All measurements shown in the figure were performed on sample A.

character—is the parent state of the superconducting and correlated insulating ground states at lower energies.

Our devices consist of hexagonal boron nitride (hBN)-encapsulated TBG[26,27], placed over a local metallic back-gate[3,4]. The main device studied in this paper (sample A, Fig. 1a) features a large (5 μm × 5 μm) area for imaging compressibility and multiple contacts for transport characterization. The results are reproduced in a second sample (sample B). The local twist angles in these samples together span a range from below to above the MA. Figure 1b shows the four-probe longitudinal resistance of sample A versus carrier density, n (controlled by the back-gate voltage, V_{BG}), and parallel magnetic field, $B_\parallel$, at a temperature of $T = 50$ mK. These measurements exhibit insulating peaks when the flat bands are completely full or empty, namely when the filling fraction $\nu \equiv n/(n_s/4)$ equals ±4 (n is the electron density, n_s corresponds to the density of four electrons per moiré unit cell), and at half-filling, $\nu = \pm 2$. Incipient superconductivity appears as resistance drops on the electron-doped side of $\nu = 2$ (up to $B_\parallel \lessapprox 0.5$ T) and on the hole-doped side of $\nu = -2$ (up to $B_\parallel \lessapprox 1$ T), similar to the observed phenomenology in MA samples[4,5]. Transport through various pairs of contacts shows spatial variations of n_s across the device, reflecting approximately 10% (0.1°) modulations of the twist angle (Supplementary Information section 5). This is confirmed more clearly by the local imaging measurements below.

Inverse compressibility is imaged with a nanotube-based scanning single electron transistor[28,29] (SET). Keeping the TBG grounded, the SET monitors the local electrostatic potential modulation above the TBG in response to back-gate voltage modulation. This yields the local inverse compressibility, $d\mu/dn$ (Supplementary Information section 2; here μ is the chemical potential). A typical trace of $d\mu/dn$ versus n, measured at $T = 4$ K and twist angle $\theta = 0.99°$ (black, Fig. 1c) features sharp $d\mu/dn$ peaks at $\nu = \pm 4$, originating from the energy gaps between the flat bands and the higher-energy bands, as well as increased $d\mu/dn$ around the CNP corresponding to Dirac-like behaviour. Integrating this curve yields μ versus n (blue, Fig. 1c), which reveals the energy gaps as jumps in μ, and the Dirac-like behaviour as a $\sqrt{n}$-like dependence around the CNP.

We characterize the varying twist angle across the sample[30,31] by spatially tracking the back-gate voltage, $V_{BG}(\mathbf{r})$, which corresponds to the $d\mu/dn$ peak at $\nu = 4$ ($\mathbf{r}$ is the spatial position). From this we deduce $n_s(\mathbf{r}) = \epsilon V_{BG}(\mathbf{r})/d$ and the local twist angle $\theta(r) = a\sqrt{n_s(r)\sqrt{3}/8}$ (d is the atomic force microscope (AFM)-measured back-gate distance, $\epsilon = 3.3 \pm 0.5$ is the hBN dielectric constant, and $a = 0.246$ nm is the graphene lattice constant). Figure 1d shows $d\mu/dn$ measured versus the spatial coordinate, Y, along a line-cut across the sample (dashed red line), and versus V_{BG}. The $\nu = 4$ peak shifts from $V_{BG} = 5.4$ V at the sample centre to $V_{BG} = 6.5$ V near its top edge, corresponding to an approximately 10% change in θ (top axis). This variation occurs in discrete steps, reflecting domains with constant θ within the sample, consistent with recent observations[31]. Mapping θ across the entire accessible area (Fig. 1e) shows a terraced θ landscape, with constant-θ domains a few hundred nanometres in size. Since our measurements are local, the variation of θ across the sample enables a systematic study of the angle dependence of the physics.

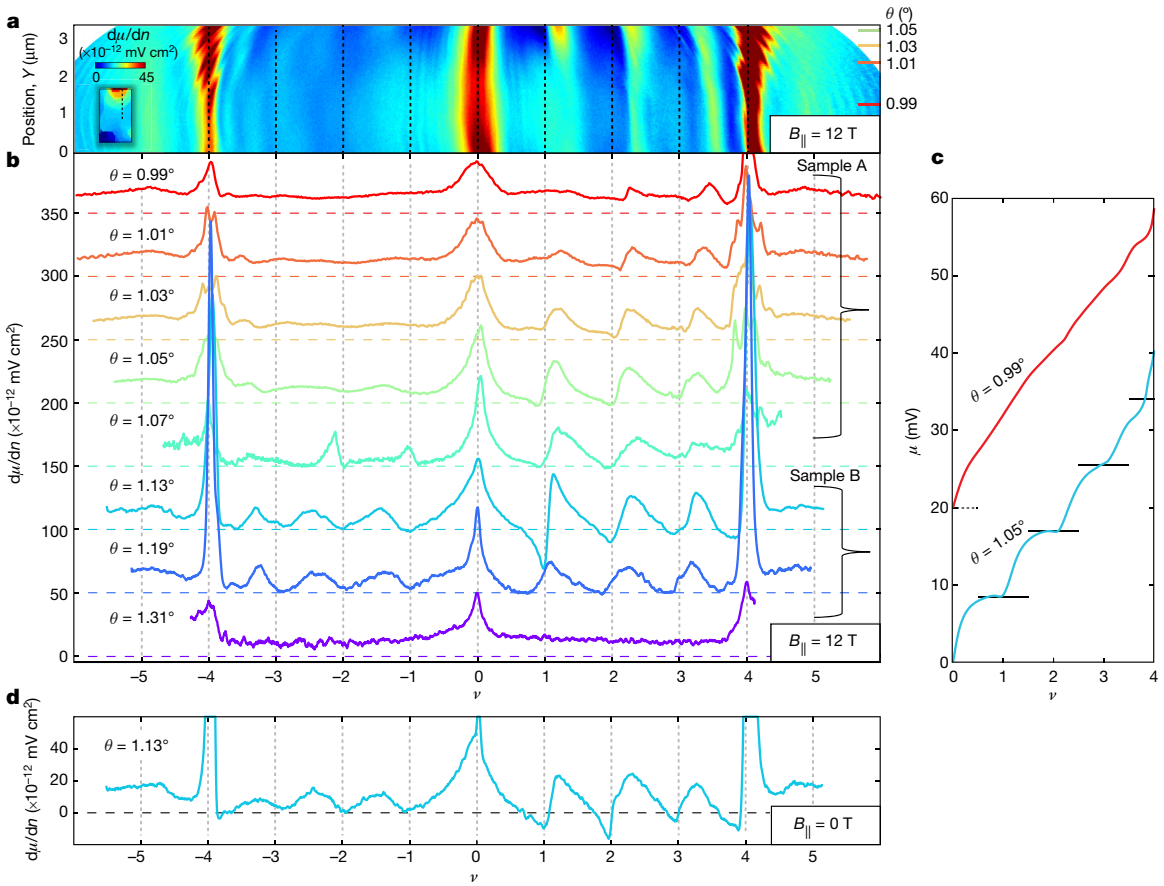

Fig. 2 | Asymmetric sawtooth features in inverse compressibility. a, $d\mu/dn$ measured as a function of ν and spatial position Y in sample A (along the same line-cut as in Fig. 1d; dashed line in the inset) at $B_{||} = 12$ T and $T = 50$ mK. The local twist angle changes along this line-cut, as indicated on the right y axis. The filling factor ν is determined by the local $n_s(Y)$. **b**, Selected $d\mu/dn$ traces from **a** (sample A, $T = 50$ mK) together with traces from sample B ($T = 4$ K), with their corresponding θ labelled (offset for clarity). An asymmetric cascade of sawtooth features is apparent, consistent between the two samples. This structure appears in a relatively narrow twist angle range around the MA. All curves are measured at $B_{||} = 12$ T apart from that of $\theta = 1.07°$, which was measured at $B_{||} = 10$ T. **c**, The chemical potential μ as function of ν, obtained by integrating the traces in **b** that correspond to $\theta = 0.99°$ and 1.05°, offset for clarity. Near the CNP, in both curves μ increases in a $\sqrt{n}$-like fashion owing to the Dirac-like dispersion. In the larger-θ curve this $\sqrt{n}$-like dependence reappears at all integer ν, demonstrating the revival of Dirac-like behaviour at the Fermi level (overall slope uncertainty is discussed in Supplementary Information section 3). The horizontal black lines are equidistant in μ. **d**, $d\mu/dn$ versus ν measured in sample B at $B_{||} = 0$ T, $T = 4$ K and $\theta = 1.13°$.

The electronic compressibility shows interesting features near integer moiré fillings, which emerge in a narrow twist angle range around the MA (Fig. 2). We first study the compressibility at finite $B_{||}$, where features at odd fillings ($\nu = 1, 3$) are strengthened, and then proceed to $B_{||} = 0$. Figure 2a plots a colour map of $d\mu/dn$, measured at $B_{||} = 12$ T, as a function of ν and the spatial coordinate, Y, along the same line-cut as in Fig. 1d. Along this line-cut, θ gradually climbs towards the MA (right y axis). We define the ν axis by separately normalizing the density at each Y with respect to the local moiré band density, $\nu = n/(n_s(Y)/4)$. Figure 2b features selected curves from this spatial evolution with $\theta = 0.99°$–$1.07°$ (offset for clarity) together with curves from sample B with $\theta = 1.13°$–$1.31°$, covering angles from below to above the MA. At $\theta = 0.99°$, $d\mu/dn$ shows a sharp jump near $\nu = 2$, and a symmetric peak above $\nu = 3$. As θ increases towards $\theta = 1.13°$, these features evolve into a cascade of asymmetric sawtooth features: approaching the integers $\nu = 1, 2, 3$ from below, $d\mu/dn$ drops gradually (to high compressibility), jumps up sharply (to low compressibility) near each integer ν, and then decreases gradually again. These asymmetric sawtooth-like features are fundamentally different from the signature of a gap, which corresponds to a jump in the chemical potential, μ, and therefore to a narrow symmetric peak in $d\mu/dn$. A similar cascade of sawtooth features appears in both samples, demonstrating the robustness of the phenomena. When the angle reaches $\theta = 1.31°$ the sawtooth features completely disappear and the compressibility is rather featureless.

We note that all the observed sawtooth features point away from the CNP. Moreover, while showing an approximate mirror symmetry about the CNP, they are clearly asymmetric with respect to the centres of the conduction and valence flat bands ($\nu = 2, -2$): $d\mu/dn$ at $|\nu| = 2 + x$ is radically different from $d\mu/dn$ at $|\nu| = 2 - x$. This emphasizes the unique role of the CNP, and strongly indicates that an asymmetry of the single-particle dispersion around the centres of the conduction and valence bands is essential for the observed asymmetry.

The high value of $d\mu/dn$ immediately after the jumps and its subsequent gradual decrease with n resemble the behaviour of $d\mu/dn$ around the CNP, suggesting a revival of Dirac-like electronic character after each integer filling. This is also apparent by comparing the $\mu(n)$ traces measured at $\theta = 0.99°$, 1.05° (Fig. 2c): at $\theta = 0.99°$, $\mu(n)$ features a $\sqrt{n}$-like dependence around the CNP, characteristic of a Dirac-like dispersion, but then climbs roughly linearly as the flat band is filled. In contrast, at $\theta = 1.05°$ a $\sqrt{n}$-like dependence re-emerges after every integer filling.

At $\nu = 2, 3$, sawtooth features appear at small θ, and as the MA is approached they increase in magnitude and move towards exact integer fillings. In contrast, the $\nu = 1, -1, -2$ sawtooth features emerge only at larger twist angles, suggesting that holes need larger θ than electrons to exhibit this behaviour.

Close to the MA the sawtooth features also appear at zero magnetic field. Figure 2d shows a $d\mu/dn$ trace measured at $\theta = 1.13°$ and $B_{||} = 0$,

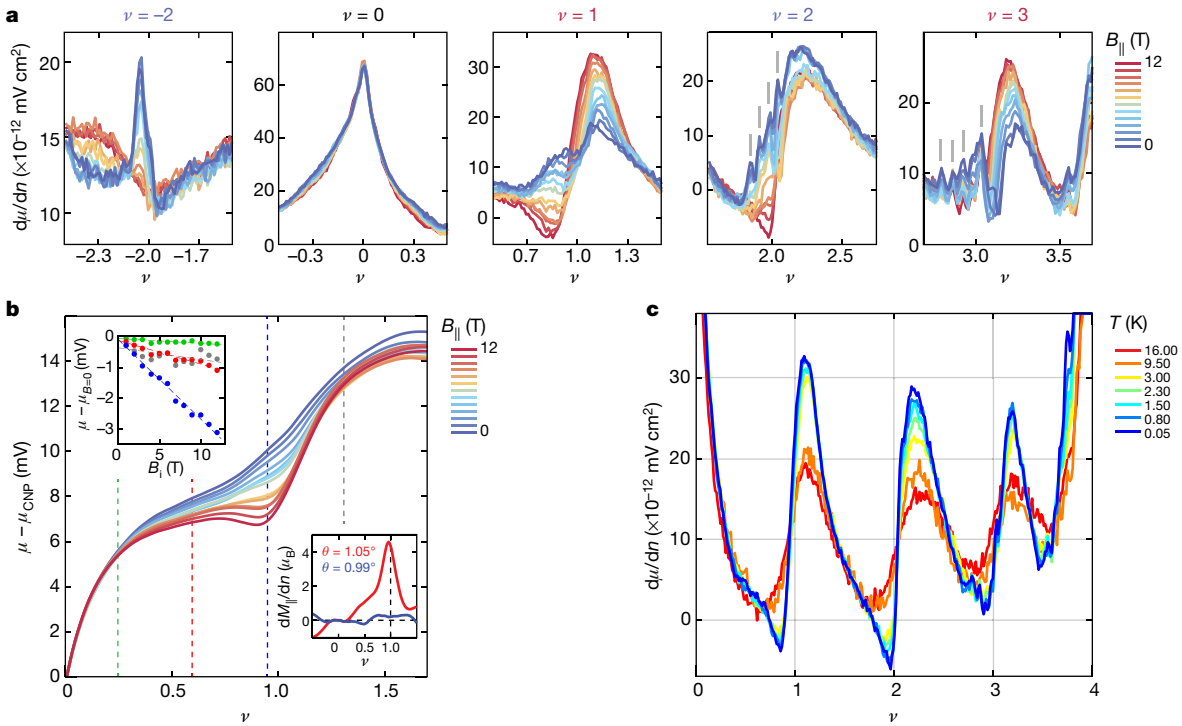

Fig. 3 | Dependence of the asymmetric sawtooth features at $\theta = 1.05°$ on parallel magnetic field and temperature. a, Parallel field dependence: shown is $d\mu/dn$ measured in sample A as a function of filling factor around $\nu = -2, 0, 1, 2, 3$ (left to right) at various values of $B_{\parallel}$ and $T = 50$ mK. (Grey lines indicate shadow sawtooth-like features arising from nearby domains with smaller twist angles that are also detected by the SET owing to its finite spatial resolution.) **b**, μ as a function of ν for various values of $B_{\parallel}$ obtained by integrating the measured $d\mu/dn$; μ is referenced to the chemical potential at the CNP, μ_{CNP}. Top inset, μ as a function of $B_{\parallel}$ at selected values of ν (green, red, blue and grey dashed lines in main panel). Bottom inset, the differential magnetization $dM_{\parallel}/dn \equiv -d\mu/dB_{\parallel}$ (extracted from a linear fit to the $B_{\parallel}$ dependence of μ at each ν) as a function of ν measured at $\theta = 1.05°$ (red) and 0.99° (blue). However, for $\theta = 0.99°$, $dM_{\parallel}/dn$ remains practically zero throughout, it peaks sharply near $\nu = 1$ for $\theta = 1.05°$, reaching a value of $(4.5 \pm 0.3)\mu_B$, signifying the build-up of spontaneous magnetization that starts around this peak. **c**, Temperature dependence: the measured $d\mu/dn$ is shown as a function of ν at various temperatures, T, at $B_{\parallel} = 12$ T.

exhibiting asymmetric sawtooth features with sharp jumps of $d\mu/dn$. Moreover, $d\mu/dn$ becomes negative before all integer fillings of the conduction flat band[32], a clear signature of strong electronic interactions.

The systematic $B_{\parallel}$ dependence of $d\mu/dn$ at $\theta = 1.05°$ is shown in Fig. 3a. $d\mu/dn$ hardly changes with $B_{\parallel}$ around the CNP, but exhibits an even–odd dependence around integer fillings: at even fillings the sawtooth weakens ($\nu = -2$) or hardly changes ($\nu = 2$) with $B_{\parallel}$, whereas at odd fillings ($\nu = 1, 3$) it strengthens with $B_{\parallel}$. This reflects alternating spin polarizations as integer fillings are crossed, consistent with previous transport observations[3–6].

The prominent magnetic-field dependence of the sawtooth feature around $\nu = 1$ allows us to study its energetics more closely. Figure 3b shows μ as a function of ν for various $B_{\parallel}$. At every ν, μ depends approximately linearly on $B_{\parallel}$, but with a different slope (Fig. 3b, top inset). By Maxwell's relation we know that $dM_{\parallel}/dn \equiv -d\mu/dB_{\parallel}$, thus these measurements allow us to determine the differential magnetization, $dM_{\parallel}/dn$, directly. Figure 3b, bottom inset, plots $dM_{\parallel}/dn$ as a function of ν for $\theta = 1.05°$ and 0.99°. At $\theta = 1.05°$, $dM_{\parallel}/dn$ is nearly zero over a finite range around $\nu = 0$, then rises slowly with ν, and near $\nu = 1$ rapidly increases to $dM_{\parallel}/dn \approx (4.5 \pm 0.3)\mu_B$, followed by a sharp drop to near zero (here μ_B is the Bohr magneton). This large $dM_{\parallel}/dn$ indicates a rapid build-up of magnetization near $\nu = 1$. The linear $B_{\parallel}$ dependence of μ, observed to the lowest $B_{\parallel}$ (Fig. 3b, top inset), suggests that the system has spontaneous magnetization near and above $\nu = 1$. In contrast, for $\theta = 0.99°$ we see that $dM_{\parallel}/dn \approx 0$ throughout the entire filling factor range (see also Supplementary Information section 8), emphasizing that the emergence of flavour symmetry breaking and magnetization near $\nu = 1$ depends sensitively on the proximity of θ to the MA.

Finally, we show the temperature dependence of $d\mu/dn$ in Fig. 3c. The sawtooth features remain strong even at the highest temperature achievable in our scanning setup, $T = 16$ K, and extrapolate to zero at $T \approx 30$ K (Supplementary Information section 12), seven times higher than the temperatures where insulating behaviour commences in transport measurements[3,5,6,33,34]. Independently, we estimate the energy scale associated with the Dirac revivals from the measured depth of the kinks in μ (Fig. 2d), obtaining $\Delta\mu \approx 4$ mV. This substantially exceeds the activation energies measured in transport[3,5,6], which were associated with correlated gaps, but is comparable to the scale over which 'strange metal' behaviour was observed in transport[33,34]. This suggests that the Dirac revivals underlie the high-energy correlated state of this system.

These robust features of the compressibility call for a theoretical understanding. Many features of our data are captured surprisingly well within a simple model that includes certain key elements but ignores many details of the complex electronic structure of the flat moiré bands. A typical calculated band structure (Fig. 4a) shows a strong asymmetry of the conduction and valence flat bands around their centres, evolving from a Dirac-like density of states (DOS) at the CNP to a massive DOS near the band edges. We believe that two features of this band structure are responsible for the observed behaviour: the strong dependence of the DOS on filling, and its inherent asymmetry about the centre of the conduction (or valence) band. We capture these features in a stripped-down model, which replaces the DOS by a linear function that terminates abruptly at the band edges (Fig. 4a, right). We assume a contact repulsive interaction, which is independent of the spin/valley flavour index, and solve the model within the Hartree–Fock approximation, allowing for spin/valley symmetry breaking via an unequal population of different flavours (see Supplementary Information sections 10, 15 for details and a discussion of the applicability and limitations of these approximations).

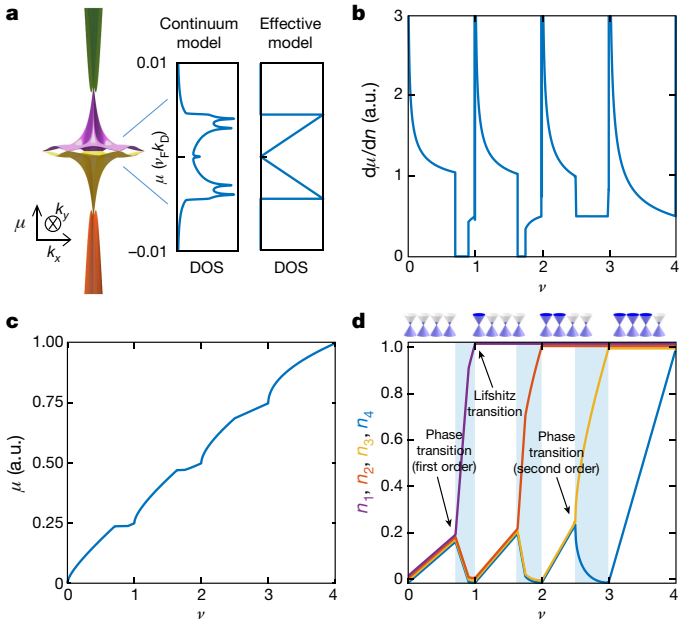

Fig. 4 | Phase transitions and Dirac revivals model. a, Band dispersion (left) and density of states (DOS; centre) of the valence and conduction flat bands, calculated from a continuum model[1,9] for a twist angle of $\theta = 1.04°$. Our theory uses a simplified version of this DOS, with a triangular energy dependence (right), capturing the two essential features of the band structure: first, the gradual increase of the DOS from a Dirac-like dispersion at the CNP to a massive dispersion at the top and bottom band edges; and second, the consequential asymmetry of this DOS around the valence and conduction band centres. **b**, Calculated $d\mu/dn$ versus ν (obtained using the Hartree–Fock approximation; see text and Supplementary Information for details), showing apparent resemblance to the measured data (for example, Fig. 2). **c**, Calculated chemical potential, μ, versus ν. **d**, The partial densities of individual flavours, n_i ($i = 1..4$) as a function of ν. The flavours start with fourfold degeneracy at charge neutrality, but then, close to an integer ν, experience a phase transition, after which one band takes all carrier from the other three (occurring in the shaded blue region). When the former band becomes full, the other three start refilling again from near the Dirac point. The beginning of this refilling corresponds to the Lifshitz transition (the jump in $d\mu/dn$, in **b**). This process repeats periodically near all integer filling factors, but each time with one less band, and can start with a first- or a second-order phase transition (arrows). The first-order transitions are followed by phase mixing regions where the partial densities interpolate linearly between those of the two phases. The flavour filling is illustrated on top (blue represents filled states).

A typical result for $d\mu/dn$ for an interaction strength comparable to the band width is shown in Fig. 4b. The resemblance to the experimental data is apparent, with asymmetric sawtooth-like features appearing at integer values of ν, preceded by sharp drops of $d\mu/dn$ to zero. The corresponding μ (Fig. 4c) also captures the main features of the experiments (Fig. 2d, c). Figure 4d shows the population of the individual flavours versus the total filling factor, revealing a cascade of phase transitions with increasing carrier density. For intermediate interaction strengths, near charge neutrality, all four flavours are populated equally. In this specific example there are first-order transitions near $\nu = 1$ and $\nu = 2$, where one flavour becomes nearly filled, while the other flavours are pushed downwards towards charge neutrality. Closely after these transitions, there are 'Lifshitz' transitions, where the filling of the majority flavour reaches 1. This Lifshitz transition explains the sawtooth features in $d\mu/dn$: before the transition, the density of states at the Fermi level is dominated by the massive majority flavour, whereas after the transition it is strongly decreased owing to the Dirac character of the remaining flavours whose occupations are reset to near the CNP. Depending on model details, the first-order and Lifshitz transitions may coincide and the majority flavour may jump directly to full filling (Supplementary Information section 11). Flavour polarization may also be initiated by a second-order transition (for example, preceding $\nu = 3$ in Fig. 4d). In our model, the sharp dips where $d\mu/dn$ approaches zero appear at the first-order phase transitions, and reflect a spatial breakup of the system into domains of the corresponding phases.

For stronger interaction, the spin/valley symmetry may be broken even at charge neutrality (see Supplementary Information section 11), but there is no corresponding evidence for that in our experiments, and thus we focus on intermediate interaction strengths, where in our model the $\nu = 0$ state is valley and spin symmetric. In the Supplementary Information we discuss extensions of this minimal model, including a more complex DOS with van Hove singularities (Supplementary Information section 12) or long-range Coulomb interactions (Supplementary Information section 16). While details of the computed $d\mu/dn$ change, the overall features remain similar to those obtained from the simple model.

Our experiments and corresponding theory predict that the flavour symmetry will be broken with a 4-, 3-, 2-, 1-fold degeneracy following fillings of $\nu = 0, 1, 2, 3$ (Supplementary Information section 17). This was indeed observed experimentally[3–6,31] (with one possible exception, above $\nu = 1$, possibly due to the rather sparse and inconclusive data). It also predicts that the Landau fans will always point away from the CNP[11], except at $\nu = 4$ where they should point towards the CNP (Supplementary Information section 17), reproducing experimental observations[3–6,31]. Another consequence of Dirac revivals is that correlated gaps will appear at integer filling only if the Dirac spectrum is gapped[11,15,17], suggesting a possible connection between a gap at the CNP and the correlated gaps at integer filling factors. From our data we can place an upper bound of approximately 1 meV on a possible thermodynamic gap hidden within our experimental resolution, consistent with the 0.14–0.9 meV activation gaps measured so far in transport[3–6].

The observed cascade of sharp asymmetric compressibility features is naturally interpreted in terms of breaking of the spin/valley symmetries at these fillings, which revives the Dirac-like character of the carriers after each transition. These features appear at temperatures far above the onset of the superconducting and correlated insulating states, indicating that the state observed here is the high-energy correlated state from which superconductors and insulators emerge at lower temperatures.

Online content

Any methods, additional references, Nature Research reporting summaries, source data, extended data, supplementary information, acknowledgements, peer review information; details of author contributions and competing interests; and statements of data and code availability are available at https://doi.org/10.1038/s41586-020-2373-y.

1. Bistritzer, R. & MacDonald, A. H. Moiré bands in twisted double-layer graphene. *Proc. Natl Acad. Sci. USA* **108**, 12233–12237 (2011).
2. Lopes dos Santos, J. M. B., Peres, N. M. R. & Castro Neto, A. H. Graphene bilayer with a twist: electronic structure. *Phys. Rev. Lett.* **99**, 256802 (2007).
3. Cao, Y. et al. Correlated insulator behaviour at half-filling in magic-angle graphene superlattices. *Nature* **556**, 80–84 (2018).
4. Cao, Y. et al. Unconventional superconductivity in magic-angle graphene superlattices. *Nature* **556**, 43–50 (2018).
5. Yankowitz, M. et al. Tuning superconductivity in twisted bilayer graphene. *Science* **363**, 1059–1064 (2019).
6. Lu, X. et al. Superconductors, orbital magnets and correlated states in magic-angle bilayer graphene. *Nature* **574**, 653–657 (2019).
7. Sharpe, A. L. et al. Emergent ferromagnetism near three-quarters filling in twisted bilayer graphene. *Science* **365**, 605–608 (2019).
8. Serlin, M. et al. Intrinsic quantized anomalous Hall effect in a moiré heterostructure. *Science* **367**, 900–903 (2020).
9. Suárez Morell, E., Correa, J. D., Vargas, P., Pacheco, M. & Barticevic, Z. Flat bands in slightly twisted bilayer graphene: tight-binding calculations. *Phys. Rev. B* **82**, 121407 (2010).
10. San-Jose, P., González, J. & Guinea, F. Non-Abelian gauge potentials in graphene bilayers. *Phys. Rev. Lett.* **108**, 216802 (2012).
11. Po, H. C., Zou, L., Vishwanath, A. & Senthil, T. Origin of Mott insulating behavior and superconductivity in twisted bilayer graphene. *Phys. Rev. X* **8**, 031089 (2018).

12. Zhang, Y.-H., Po, H. C. & Senthil, T. Landau level degeneracy in twisted bilayer graphene: role of symmetry breaking. *Phys. Rev. B* **100**, 125104 (2019).
13. Liu, S., Khalaf, E., Lee, J. Y. & Vishwanath, A. Nematic topological semimetal and insulator in magic angle bilayer graphene at charge neutrality. Preprint at http://arXiv.org/abs/1905.07409 (2019).
14. Po, H. C., Zou, L., Senthil, T. & Vishwanath, A. Faithful tight-binding models and fragile topology of magic-angle bilayer graphene. *Phys. Rev. B* **99**, 195455 (2019).
15. Xie, M. & MacDonald, A. H. Nature of the correlated insulator states in twisted bilayer graphene. *Phys. Rev. Lett.* **124**, 097601 (2020).
16. Isobe, H., Yuan, N. F. Q. & Fu, L. Unconventional superconductivity and density waves in twisted bilayer graphene. *Phys. Rev. X* **8**, 041041 (2018).
17. Ochi, M., Koshino, M. & Kuroki, K. Possible correlated insulating states in magic-angle twisted bilayer graphene under strongly competing interactions. *Phys. Rev. B* **98**, 081102 (2018).
18. Li, G. et al. Observation of Van Hove singularities in twisted graphene layers. *Nat. Phys.* **6**, 109–113 (2010).
19. Brihuega, I. et al. Unraveling the intrinsic and robust nature of van Hove singularities in twisted bilayer graphene by scanning tunneling microscopy and theoretical analysis. *Phys. Rev. Lett.* **109**, 196802 (2012).
20. Wong, D. et al. Local spectroscopy of moiré-induced electronic structure in gate-tunable twisted bilayer graphene. *Phys. Rev. B* **92**, 155409 (2015).
21. Tomarken, S. L. et al. Electronic compressibility of magic-angle graphene superlattices. *Phys. Rev. Lett.* **123**, 046601 (2019).
22. Kerelsky, A. et al. Maximized electron interactions at the magic angle in twisted bilayer graphene. *Nature* **572**, 95–100 (2019).
23. Choi, Y. et al. Electronic correlations in twisted bilayer graphene near the magic angle. *Nat. Phys.* **15**, 1174–1180 (2019); erratum **15**, 1205 (2019).
24. Xie, Y. et al. Spectroscopic signatures of many-body correlations in magic-angle twisted bilayer graphene. *Nature* **572**, 101–105 (2019).
25. Jiang, Y. et al. Charge order and broken rotational symmetry in magic-angle twisted bilayer graphene. *Nature* **573**, 91–95 (2019).
26. Cao, Y. et al. Superlattice-induced insulating states and valley-protected orbits in twisted bilayer graphene. *Phys. Rev. Lett.* **117**, 116804 (2016).
27. Kim, K. et al. van der Waals heterostructures with high accuracy rotational alignment. *Nano Lett.* **16**, 1989–1995 (2016).
28. Waissman, J. et al. Realization of pristine and locally tunable one-dimensional electron systems in carbon nanotubes. *Nat. Nanotechnol.* **8**, 569–574 (2013).
29. Honig, M. et al. Local electrostatic imaging of striped domain order in $LaAlO_3/SrTiO_3$. *Nat. Mater.* **12**, 1112–1118 (2013).
30. Yoo, H. et al. Atomic and electronic reconstruction at the van der Waals interface in twisted bilayer graphene. *Nat. Mater.* **18**, 448–453 (2019).
31. Uri, A. et al. Mapping the twist-angle disorder and Landau levels in magic-angle graphene. *Nature* **581**, 47–52 (2020).
32. Eisenstein, J., Pfeiffer, L. & West, K. Negative compressibility of interacting two-dimensional electron and quasiparticle gases. *Phys. Rev. Lett.* **68**, 674–677 (1992).
33. Cao, Y. et al. Strange metal in magic-angle graphene with near Planckian dissipation. *Phys. Rev. Lett.* **124**, 076801 (2020).
34. Polshyn, H. et al. Large linear-in-temperature resistivity in twisted bilayer graphene. *Nat. Phys.* **15**, 1011–1016 (2019).

Data availability

The data that support the plots and other analysis in this work are available from the corresponding author upon request.

Code availability

The code used in this work is available at https://github.com/erezberg/Dirac_revivals_theory/ .

Acknowledgements We thank U. Aviram, A. H. Macdonald, J. Ruhman, H. Steinberg, S. Todadri, A. Yacoby and E. Zeldov for their suggestions. Work at Weizmann was supported by a Leona M. and Harry B. Helmsley Charitable Trust grant, ISF grants (712539 and 13335/16), a Deloro award, the Sagol Weizmann-MIT Bridge programme, the ERC-Cog (See-1D-Qmatter, no. 647413), ISF Research Grants in the Quantum Technologies and Science Program (994/19 and 2074/19), the DFG (CRC/Transregio 183), the ERC-Cog (HQMAT, no. 817799), EU Horizon 2020 (LEGOTOP 788715) and the Binational Science Foundation (NSF/BMR-BSF grant 2018643). Work at MIT was supported by the National Science Foundation (DMR-1809802), the Center for Integrated Quantum Materials under NSF grant DMR-1231319, and the Gordon and Betty Moore Foundation's EPiQS Initiative through grant GBMF4541 to P.J.-H. for device fabrication, transport measurements and data analysis. This work was performed in part at the Harvard University Center for Nanoscale Systems (CNS), a member of the National Nanotechnology Coordinated Infrastructure Network (NNCI), which is supported by the National Science Foundation under NSF ECCS award no. 1541959. D.R.-L. acknowledges partial support from Fundaciòn Bancaria 'la Caixa' (LCF/BQ/AN15/10380011) and from the US Army Research Office (grant no. W911NF-17-S-0001). K.W. and T.T. acknowledge support from the Elemental Strategy Initiative conducted by the MEXT, Japan, A3 Foresight by JSPS and the CREST (JPMJCR15F3), JST.

Author contributions U.Z., A.R., D.R.-L., P.J.-H. and S.I. designed the experiment. U.Z. and A.R. performed the experiments. D.R.-L. and Y.C. fabricated the twisted bilayer graphene devices. U.Z., A.R. and S.I. analysed the data. R.Q., A.R., F.v.O., Y.O., A.S. and E.B. formulated the theory and performed the Hartree-Fock calculations. K.W. and T.T. supplied the hBN crystals. U.Z., A.R., D.R.-L., A.S., E.B., P.J.-H. and S.I. wrote the manuscript, with input from all authors.

Competing interests The authors declare no competing interests.

Additional information
Supplementary information is available for this paper at https://doi.org/10.1038/s41586-020-2373-y.
Correspondence and requests for materials should be addressed to P.J.-H. or S.I.
Peer review information *Nature* thanks Ivan Brihuega, Fan Zhang and Klaus Ensslin for their contribution to the peer review of this work.
Reprints and permissions information is available at http://www.nature.com/reprints.